

Oxidative stress-induced intervertebral disc remodelling and elevated stiffness drive idiopathic scoliosis in preclinical models

Received: 26 August 2024

Accepted: 21 August 2025

Published online: 30 September 2025

 Check for updates

Patrick G. Pumputis^{1,2,9}, Ran Xu^{1,2,9}, Josh Gopaul^{3,9}, Arash Panahifar^{4,5}, Vida Erfani^{1,2}, Jenica L. M. Van Gennip¹, B. Frank Eames⁶, Nikan Fakhari^{3,7}, Jerome Baranger³, David E. Lebel⁸, Olivier Villemain^{3,7}✉ & Brian Ciruna^{1,2}✉

Adolescent idiopathic scoliosis (AIS) is the most prevalent pediatric spine disorder, developing in the absence of obvious physiological defects. Genome sequencing and functional studies have demonstrated association of musculoskeletal collagen variants and cartilaginous extracellular matrix (ECM) defects in a subset of patients. However, the underlying biological causes of AIS remain poorly understood, limiting treatment options. Using multiple zebrafish AIS models, we demonstrate that reduction-oxidation (redox) imbalances induce cell stress and collagen remodelling within intervertebral segments of the developing spine. Mutant spines are consequently stiffer, as measured by shear wave elastography, and exhibit deformations of intervertebral structures. Remarkably, elevated stiffness and intervertebral ECM phenotypes are detectable prior to scoliosis onset, suggesting a causal relationship, and can be suppressed by antioxidant treatment. Together, our preclinical studies implicate oxidative stress-induced intervertebral deformations in the pathogenesis of AIS and identify elevated spine stiffness and redox imbalance as plausible first-in-kind prognostic biomarkers and therapeutic targets.

Adolescent idiopathic scoliosis (AIS) is a common pediatric disorder characterized by lateral and rotational deviations in the spinal column that develop in the absence of obvious congenital or physiological defects¹. AIS afflicts 3–4% of children worldwide yet underlying causes are poorly understood, in part due to genetic heterogeneity and suspected environmental influences¹. Patient genome sequencing and functional genetic studies have implicated a diverse group of AIS-associated variants in scoliosis, with gene functions ranging from musculoskeletal collagen and cartilaginous extracellular matrix (ECM) formation^{2–4}, neuromuscular development⁵, planar cell polarity⁶, cilia

function⁷, carbohydrate metabolism⁸, synaptic neurotransmission and central pattern generators⁹. However, over 95% of total causative genetic variance in AIS is thought to remain unknown¹⁰. Because most AIS etiological studies involve patients with established scoliotic curves, determining a biological mechanism of cause and effect is particularly challenging, and treatment options remain limited to mechanical interventions like bracing or invasive corrective surgery¹.

Zebrafish have emerged as powerful experimental models for dissecting complex biological mechanisms associated with AIS^{11,12}. It was discovered that neuroinflammatory signals and oxidative stress,

¹Developmental & Stem Cell Biology Program, The Hospital for Sick Children, Toronto, ON, Canada. ²Department of Molecular Genetics, University of Toronto, Toronto, ON, Canada. ³Translational Medicine Program, The Hospital for Sick Children, Toronto, ON, Canada. ⁴BioMedical Imaging and Therapy Beamline, Canadian Light Source, Saskatoon, SK, Canada. ⁵Department of Medical Imaging, College of Medicine, University of Saskatchewan, Saskatoon, SK, Canada. ⁶Department of Anatomy, Physiology, and Pharmacology, University of Saskatchewan, Saskatoon, SK, Canada. ⁷Department of Medical Biophysics, University of Toronto, Toronto, ON, Canada. ⁸Division of Orthopaedic Surgery, The Hospital for Sick Children, Toronto, ON, Canada. ⁹These authors contributed equally: Patrick G. Pumputis, Ran Xu, Josh Gopaul. ✉e-mail: olivier.villemain@chu-bordeaux.fr; ciruna@sickkids.ca

arising from imbalances in cerebrospinal fluid (CSF) homeostasis, are both necessary and sufficient to cause AIS-like spinal curvatures in zebrafish^{13–15}. Furthermore, treatment with antioxidant and immunomodulating compounds like N-acetylcysteine (NAC) or NAC-ethyl ester (NACET, a more bioavailable form of NAC) can suppress scoliosis onset and severe spinal curve progression in zebrafish models^{14–16}. While this provides proof-of-principle that scoliosis might be managed therapeutically, the undetermined mechanisms by which oxidative stress leads to spinal curvature and their relevance to human AIS pose a barrier to clinical translation.

Here, we interrogate the downstream causes of scoliosis in the dominant *SCO-spondin* (*sspo*^{*dmh4/+*}) mutant zebrafish model of AIS¹⁵. These fish develop idiopathic-like spinal curvatures in response to ox-inflammatory signals that are linked to the disruption of Reissner's fiber (RF), a proteinaceous filament that threads through ventricular cavities of the spinal cord and brain. We demonstrate that abnormal axial reduction-oxidation (redox) states in *sspo*^{*dmh4/+*} mutants induce both intervertebral collagen ECM remodelling defects and elevated spine stiffness that appear causally linked to the onset and progression of scoliosis. Furthermore, we characterize resulting intervertebral disc (IVD) deformations as pathophysiological defects shared between multiple additional zebrafish scoliosis models and human AIS patients. Although the clinical relevance of these findings remains to be determined, if translatable, we provide evidence that elevated spine stiffness and oxidative stress may prove valuable, first-in-kind, prognostic biomarkers and therapeutic targets for idiopathic scoliosis.

Results

sspo^{*dmh4/+*} mutants exhibit an elevated oxidative state in proximity to the developing spine

NACET, a potent antioxidant, can suppress the onset and severe progression of scoliosis in *sspo*^{*dmh4/+*} AIS models¹⁵. To investigate how oxidative stress may influence spine development, we characterized the spatial distribution of reduction-oxidation (redox) imbalance in larval zebrafish using the cell-permeable fluorescent redox probe 2',7'-dichlorofluorescein diacetate (DCFH-DA)¹⁷. While the probe cannot attribute redox changes to specific reactive oxygen species (ROS), it can be used as a general indicator of redox state¹⁷. Staining was performed on wildtype (WT) and *sspo*^{*dmh4/+*} zebrafish at 10 days post fertilization (dpf) and 6 mm standard length (SL), prior to scoliosis onset. At this stage, *sspo*^{*dmh4/+*} zebrafish appear morphologically indistinguishable from WT (Fig. 1a, b). However, elevated oxidation levels were detected in the dorsal telencephalon and cranial vessels of *sspo*^{*dmh4/+*} mutants (Fig. 1c, e and Supplementary Fig. 1b), adjacent to the diencephalic choroid plexus and in close proximity to the subcommissural organ (SCO), which is the site of abnormal SCO-spondin secretion in mutant animals¹⁵.

Notably, neuroinflammation and elevated TNF α reporter expression were previously identified in the brain of *sspo*^{*dmh4/+*} mutants at 21 dpf¹⁵. To examine the relationship between inflammation and redox imbalance, we imaged the TNF α reporter¹⁸ at earlier stages of development. At 10 dpf, no significant difference in TNF α reporter expression was observed in the dorsal telencephalon, despite the presence of elevated ROS in *sspo*^{*dmh4/+*} mutants (Supplementary Fig. 2). However, a significant elevation in TNF α reporter activity was observed within macrophages of the telencephalon at 14 dpf, as identified by co-labeling with the *Tg(mpeg1:mCherry)* macrophage reporter¹⁹ (Supplementary Fig. 3). These results indicate that redox imbalance precedes inflammation in the brain of *sspo*^{*dmh4/+*} mutant animals.

Strikingly, elevated oxidative signals were also observed along the trunk of 10 dpf *sspo*^{*dmh4/+*} zebrafish in the spinal cord, trunk vasculature and dorsal aorta, as well as in discrete peri-notochordal segments (Fig. 1d, f, m and Supplementary Fig. 1a, c, d, e). These segments correspond to developing cartilaginous intervertebral domains of the spine, as demonstrated by the complementary pattern of *TgBAC(entpd5a::pkRed)* reporter expression²⁰ in alternating mineralizing

domains (Supplementary Fig. 1f, g). In contrast, no difference in DCFH-DA signals was observed in the trunk muscle (myotome) of 10 dpf WT and *sspo*^{*dmh4/+*} zebrafish (Supplementary Fig. 1h, i). Treatment with 500 μ M of NACET from 5 to 10 dpf led to the suppression of the DCFH-DA signal in *sspo*^{*dmh4/+*} mutants at 10 dpf, supporting that elevated DCFH-DA staining is caused by an increase in oxidative state (Supplementary Fig. 1j).

Prior to scoliosis onset, we observed a large distribution of DCFH-DA staining levels within 10 dpf *sspo*^{*dmh4/+*} zebrafish cohorts (Fig. 1m). Noting that scoliosis is not fully penetrant in *sspo*^{*dmh4/+*} mutants, and can vary widely between clutches (average penetrance of 57.2% and standard deviation of \pm 29.7%; Supplementary Fig. 1k), we next asked if differences in redox imbalance correlate with scoliosis development (typically between 14–16 dpf, Fig. 1g, h). Remarkably, DCFH-DA staining was even more pronounced in scoliotic *sspo*^{*dmh4/+*} zebrafish at 14 dpf, and was not observed in non-scoliotic *sspo*^{*dmh4/+*} mutants (Fig. 1i–l, n–p and Supplementary Fig. 1l, m). These results support a causal relationship between redox imbalance and spinal curvature.

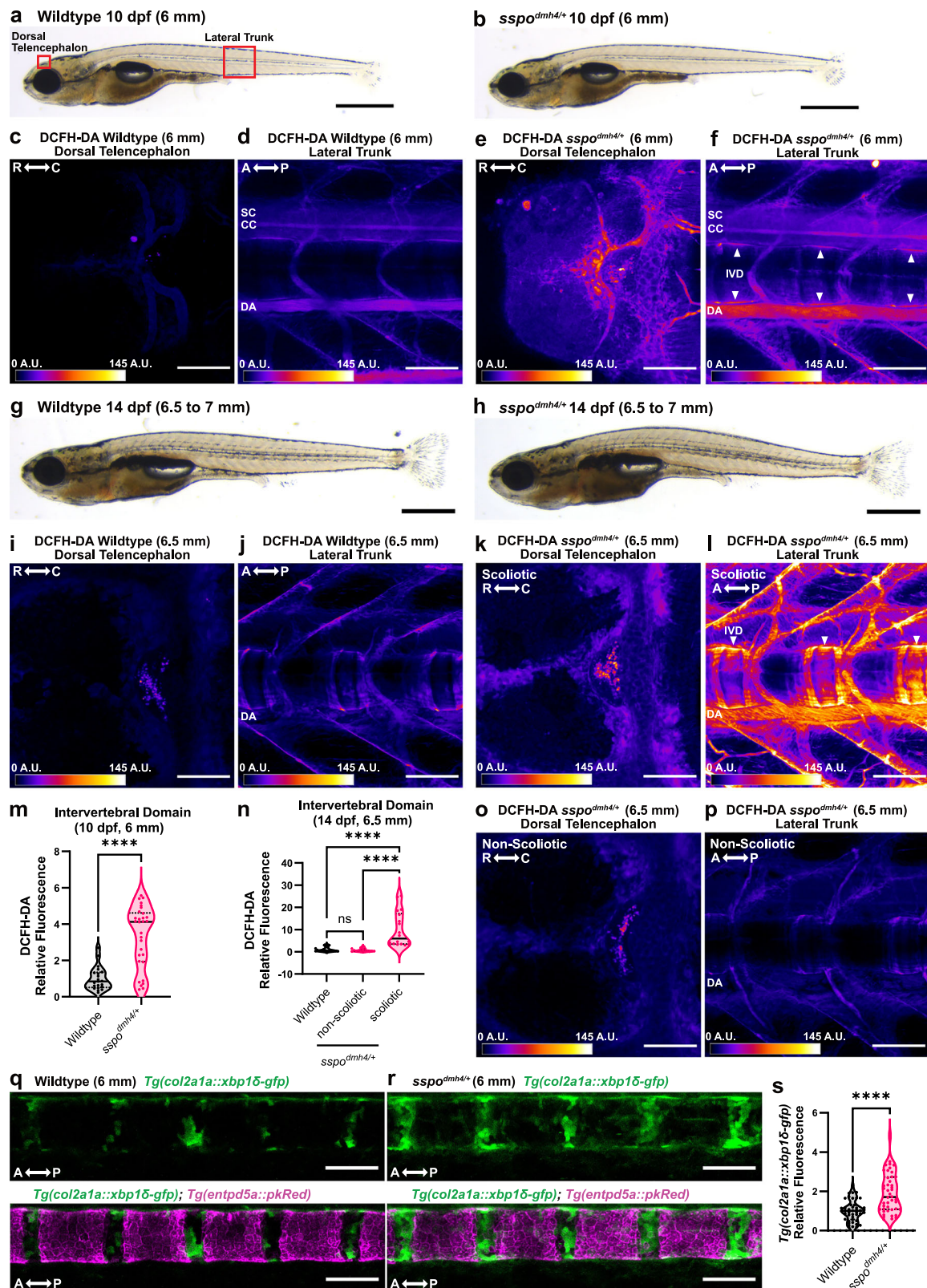
To determine whether redox imbalance represents a generalizable feature of zebrafish scoliosis, or a property specific to *sspo*^{*dmh4/+*} mutants, we performed DCFH-DA staining on two additional AIS models (*katnb1* and *vangl2*) that share upstream CSF homeostasis defects but differ in underlying molecular genetic causes^{21,22}. Staining was performed on 14 dpf *katnb1* and 5 dpf *vangl2* mutants, shortly after the onset of scoliosis in the respective models. Stronger oxidation states were also observed within the central nervous system and axial midline/trunk of *katnb1* and *vangl2* mutants, compared with sibling controls (Supplementary Figs. 4 and 5). Overall, these data suggest that redox imbalance precedes neuroinflammation and scoliosis onset in *sspo*^{*dmh4/+*} mutants, and that elevated ROS in close juxtaposition to the developing spine is associated with spinal curve progression across diverse zebrafish models of AIS.

Redox imbalance induces endoplasmic reticulum (ER) stress within intervertebral segments

The zebrafish notochord, comprised of inner vacuolated cells and outer peri-notochordal sheath cells, provides structural support to the embryo and serves as a template for spine development¹¹. Sheath cells, abundant in rough ER, are secretory cells that contribute to the notochord's ECM-rich lamellar sheath¹¹, which segments into developing vertebrae and IVDs²⁰. Since dysregulation of redox homeostasis in cells can initiate ER stress and an unfolded protein response (UPR)²³, we hypothesized that peri-notochordal accumulation of ROS in *sspo*^{*dmh4/+*} IVD segments may induce ER stress and negatively impact sheath cell function.

To assess ER stress in *sspo*^{*dmh4/+*} mutants, we modified an established transgenic assay that incorporates an IRE1 endonuclease-catalyzed splicing cassette that reports on XBP1 activation via expression of a functionally inert XBP1spliced(δ)-GFP fusion protein (Supplementary Fig. 6a)²⁴. Specifically, the *xbp1 δ -eGFP* ER stress reporter was cloned downstream of a *col2a1a* promoter²⁵ to direct expression within cartilaginous IVD segments and the site of observed oxidation (arrowheads, Fig. 1f, l). Basal levels of *Tg(col2a1a::xbp1 δ -eGFP)* reporter activity and ER stress could be detected within developing IVDs of WT fish (10 dpf, 6 mm SL) (Fig. 1q) in between alternating mineralizing domains labeled by *TgBAC(entpd5a::pkRed)*²⁰. Strikingly, a significant increase in *Tg(col2a1a::xbp1 δ -eGFP)* reporter activity was observed within IVDs of *sspo*^{*dmh4/+*} mutant zebrafish (10 dpf, 6 mm SL) (Fig. 1r, s). Importantly, the elevated reporter activity is not due to changes in *col2a1a* promoter activity in *sspo*^{*dmh4/+*} mutants, as no differences in the expression of a *TgBAC(col2a1a::eGFP)* reporter²⁶ construct were observed in 10 dpf *sspo*^{*dmh4/+*} mutants compared to wildtype IVDs (Supplementary Fig. 6b–d). Overall, these results indicate an active ER stress response prior to the onset of scoliosis.

To determine whether observed ER stress was linked to oxidative stress, zebrafish were treated with 500 μ M of NACET from 5 to 10 dpf.



NACET treatment had no effect on *Tg(col2a1a::xbp1δ-eGFP)* reporter activity in wildtype zebrafish, but fully suppressed ER stress responses in *sspo*^{dmh4/+} mutant zebrafish to wildtype levels (Supplementary Fig. 6e–i). Together, these data indicate that redox imbalances induce ER stress within the IVDs of *sspo*^{dmh4/+} mutant animals preceding scoliosis onset. Although perdurance of the XBP1δ-GFP reporter protein

confounds precise assessment of the acuteness of observed ER stress responses, the response was transient in nature as no difference in *Tg(col2a1a::xbp1δ-eGFP)* reporter activity was observed in *sspo*^{dmh4/+} mutant scoliotic zebrafish at 14 dpf compared to WT (6.5 mm SL; Supplementary Fig. 6j–l), despite persistence of redox imbalance in *sspo*^{dmh4/+} scoliotic zebrafish at this stage (Fig. 11).

Fig. 1 | IVD redox imbalance and ER stress precede idiopathic-like scoliosis.

a, b Lateral whole-mount images of 10 dpf (6 mm SL) wildtype (**a**) and *sspo^{dmh4/+}* mutant (**b**) zebrafish. Red boxes indicate regions imaged by confocal microscopy. Scale bars = 1 mm. **c–f** Confocal images of DCFH-DA staining of the dorsal telencephalon (**c, e**) and lateral trunk (**d, f**) of 10 dpf (6 mm SL) wildtype (**c, d**) and *sspo^{dmh4/+}* mutant (**e, f**) zebrafish. Scale bars = 100 μ m. **g, h** Lateral whole-mount images of 14 dpf (6.5 to 7 mm SL) wildtype (**g**) and scoliotic *sspo^{dmh4/+}* mutant (**h**) zebrafish. Scale bars = 1 mm. **i–l, o, p** Confocal images of DCFH-DA staining of the dorsal telencephalon (**i, k, o**) and lateral trunk (**j, l, p**) of 14 dpf (6.5 mm SL) wildtype (**i, j**) and scoliotic (**k, l**) and non-scoliotic (**o, p**) *sspo^{dmh4/+}* mutant zebrafish. **m, n** Relative fluorescence quantification of DCFH-DA staining of intervertebral domains, all showing significantly increased oxidative state in *sspo^{dmh4/+}* mutant zebrafish at 10 dpf (**m**, WT $N = 7$ fish, $n = 21$ IVDs, *sspo^{dmh4/+}* $N = 10$ fish, $n = 30$ IVDs) and only in scoliotic mutants at 14 dpf (**n**, WT $N = 6$ fish, $n = 18$ IVDs, *sspo^{dmh4/+}* non-

scoliotic $N = 5$ fish, $n = 15$ IVDs, *sspo^{dmh4/+}* scoliotic $N = 6$ fish, $n = 18$ IVDs). Lookup tables arbitrary units (A.U.) are 0 to 145. IVD intervertebral domain, DA dorsal aorta, CC central canal, SC spinal cord. Arrowheads indicate increased oxidative state along developing intervertebral domains. **q, r** Confocal images of *Tg(col2a1a::xbp1b-gfp)* reporter expression in 10 dpf (6 mm SL) wildtype (**q**) and *sspo^{dmh4/+}* (**r**) zebrafish, demonstrating an elevated ER stress response within the intervertebral domains of *sspo^{dmh4/+}* mutants, prior to the onset of scoliosis. Scale bar = 100 μ m. **s** Relative fluorescence quantification of *Tg(col2a1a::xbp1b-gfp)* reporter expression within intervertebral domains ($N = 11$, $n = 44$ IVDs for each genotype), demonstrating elevated ER stress in *sspo^{dmh4/+}* mutants. Violin plots show all data points, median (solid line), and quartiles (dotted line). Data were analyzed by a two-sided Mann–Whitney test (**m, s**) or a Kruskal–Wallis test followed by a Dunn's multiple comparison test (**n**). **** $p \leq 0.0001$. Source data are provided as a Source Data file.

***sspo^{dmh4/+}* mutants exhibit IVD deformations and collagen ECM defects**

To further investigate the functional consequence of oxidative stress on zebrafish IVD development, we performed high-resolution synchrotron-based X-ray micro-computed tomography (synchrotron μ CT) on juvenile fish at 21 dpf (10 mm SL), when spinal curvature is well-established in *sspo^{dmh4/+}* AIS models (Supplementary Fig. 7). Samples were stained using a diffusible iodine-based contrast enhancement, and 4–5 segments of the caudal spine were imaged at 0.36 μ m voxel size to produce high-resolution 3D datasets of the mineralized skeleton and surrounding soft tissues (Fig. 2a, e and Supplementary Videos 1–4). At the stages analyzed, zebrafish IVDs have differentiated into two principal structures (Figs. 3a and 4a, b). These include an inner domain comprised of vacuolated and sheath notochordal cells; and an outer intervertebral ligament (IVL) that physically connects two adjacent vertebral bodies, comprised of layered collagen type II and elastin matrix, dense collagen type I matrix and collagen type I bundle fibers²⁷. These inner and outer intervertebral structures are functionally analogous to the nucleus pulposus (NP) and annulus fibrosus (AF) layers of the human IVD, respectively^{27–29}.

Remarkably, the IVL (AF) of *sspo^{dmh4/+}* mutants exhibited obvious structural defects and appeared highly deformable. In wildtype zebrafish, the IVL could be identified connecting two adjacent vertebral bodies, looping outward in the coronal plane towards neighboring muscle fibers (arrowhead, Fig. 2b). This organization of IVL structure, previously described for wildtype adult zebrafish^{27,28}, was stable across the circumference of the IVD (Fig. 2c–c'''; Supplementary Video 5) with its dense collagen layer appearing in transverse sections as a smooth and regular band of high-contrast, circling the periphery of the intervertebral segment (arrowhead, Fig. 2d). In contrast, coronal images of *sspo^{dmh4/+}* mutants often demonstrated an inversion of typical AF structure, with sections of *sspo^{dmh4/+}* IVL folding interiorly towards the NP cell layers (arrowhead, Fig. 2f). Strikingly, the contour of *sspo^{dmh4/+}* IVL layers exhibited significant deformations over short distances (Fig. 2g–g''') and, in some instances, could be observed transitioning between wildtype and inverted orientations within 30 μ m intervals (Supplementary Videos 6, 7). As a result, transverse sections of *sspo^{dmh4/+}* mutants exhibited irregular and twisted IVL borders (arrows, Fig. 2h) displaced towards the interior of the intervertebral AF layer (arrowhead, Fig. 2h).

Similar IVL deformations were observed upon histological analysis (H&E and Picrosirius red staining) of formalin-fixed paraffin-embedded 21 dpf *sspo^{dmh4/+}* spines (Fig. 3b–f). Notably, histology protocols had a profound effect on resulting IVL morphology, as use of formic acid (a stringent decalcifying agent) resulted in inverted or deformed IVLs in 100% of both *sspo^{dmh4/+}* and WT intervertebral segments (Fig. 3b–d). In contrast, use of EDTA decalcification protocols yielded IVL deformations in only 18% of WT IVD segments (Fig. 3b, e), whereas 92% of *sspo^{dmh4/+}* IVDs exhibited IVL inversion (Fig. 3b, f), consistent with synchrotron μ CT analyses. Furthermore, an increased

occurrence of IVL deformation was also observed in 21 dpf *vangl2* and 30 dpf *katnb1* mutants when compared to their normal sibling controls (Fig. 3b, g–j), supporting IVL defects as a shared phenotype across genetically diverse AIS models.

Formic acid has been documented to degrade ECM peptides and cause increased distortion to ECM morphology^{30,31}, implicating ECM remodelling as a possible mechanism underlying IVL deformity. To probe the structural integrity of the IVD matrix in *sspo^{dmh4/+}* mutants, we performed collagen-hybridizing peptide (CHP) stains on axial skeleton preparations of juvenile fish at 21 dpf (10 mm SL). CHP is a synthetic construct that mimics the helical structure of endogenous collagen peptides and can bind to open regions in collagen triple helices to report on collagen ECM damage and remodelling (Fig. 4c)³². CHP staining appeared stronger in *sspo^{dmh4/+}* mutant IVLs compared to wildtype, and highlighted irregularities in IVL structure (arrows, Fig. 4d–g) previously observed in μ CT images. Furthermore, brighter and ectopic CHP signals were also observed within the NP layer of *sspo^{dmh4/+}* mutants (arrowheads, Fig. 4d–g), indicating extensive damage to the collagen matrix, dysregulated ECM remodelling, or both. These data demonstrate abnormalities in the structural properties of the IVDs in zebrafish AIS models, both at the morphological and molecular levels.

Zebrafish AIS models exhibit stiffer spines

Viscoelastic properties of AIS patient intervertebral disc tissues have also been reported to be significantly altered. Specifically, the AF is stiffer in AIS patients compared to healthy controls, as measured by shear wave elastography (SWE)^{33,34}. SWE uses an acoustic radiation force to induce mechanical tissue displacement and calculates the velocity of shear waves propagating in the orthogonal direction. As tissue stiffness is directly proportional to shear wave speed, this provides a quantitative measure of tissue elasticity^{35,36}. To further characterize physiological defects associated with oxidative stress and scoliosis in our models, we utilized SWE to quantitatively assess zebrafish spine stiffness (Supplementary Fig. 8a–c).

To begin, we conducted SWE at 16 dpf (average SL = 7.1 \pm 0.2 mm) and 21 dpf (average SL = 8.9 \pm 0.6 mm) stages, corresponding to the onset and progression of scoliosis in *sspo^{dmh4/+}* mutants, respectively (Fig. 5a, b). Euthanized zebrafish were embedded in low-melting agarose, and SWE was performed on the abdominal segment of the spine (note that variations in SWE 'push' locations and agarose density did not significantly alter shear wave velocities; Supplementary Fig. 8d, e). Remarkably, *sspo^{dmh4/+}* shear wave velocities were significantly faster than wildtype controls at both time points (Fig. 5c, d), indicating an increase in spine stiffness in scoliotic *sspo^{dmh4/+}* mutant zebrafish. Observed increases in spine stiffness were not likely caused by changes in vertebral bone density, as μ CT analysis of the mineralized axial skeleton of adult zebrafish did not reveal significant differences in *sspo^{dmh4/+}* tissue mineral density compared to wildtype siblings (Supplementary Fig. 9).

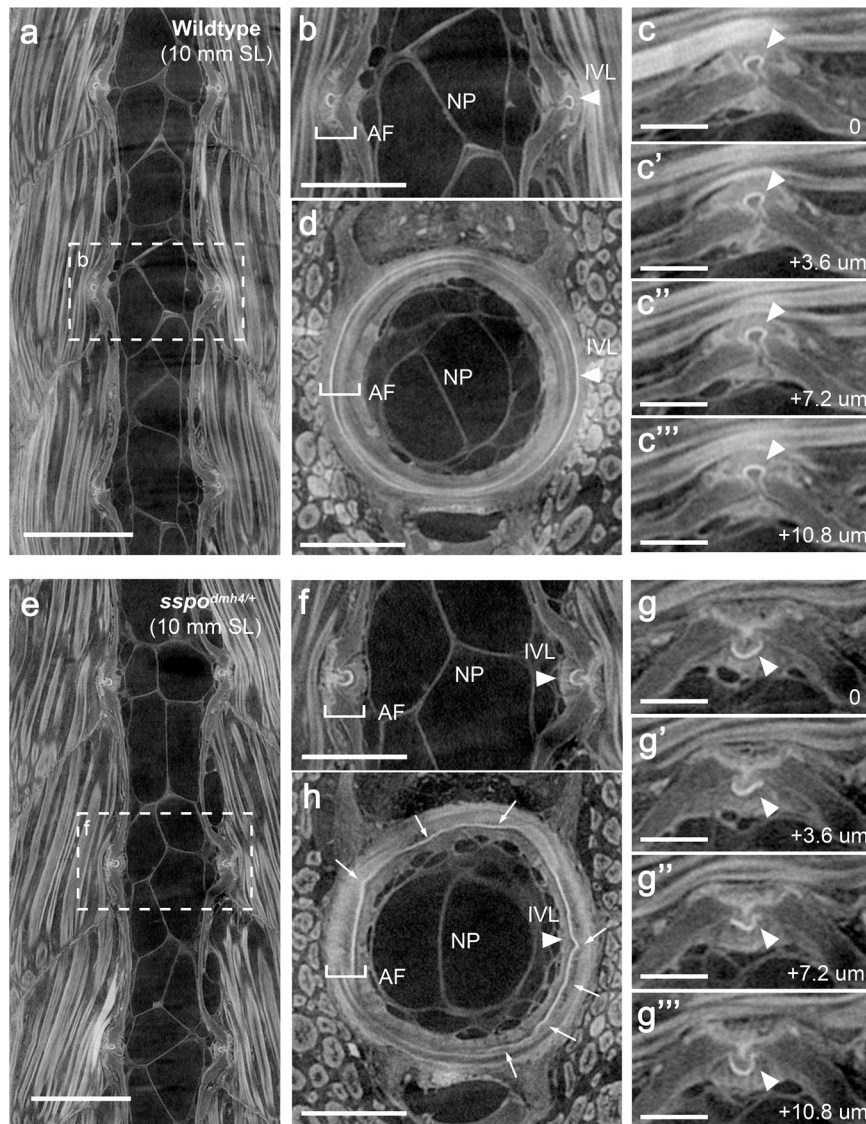


Fig. 2 | Scoliotic fish exhibit intervertebral ligament deformations. **a–g** High-resolution synchrotron-based X-ray micro-computed tomography (μ CT) imaging of iodine contrast-stained wildtype (**a–d**) and *sspo*^{dmh4/+} mutant (**e–h**) juvenile fish at 21 dpf (10 mm SL). Representative sections from coronal (**a–c**, **e–g**) and transverse (**d**, **h**) planes are shown. Dashed boxes (**a**, **e**) indicate featured intervertebral segments. Arrowheads (**b–d**, **f–h**) indicate the intervertebral ligament, which loops outward toward neighboring musculature in wildtype animals ($N = 3$ fish, $n = 13$ IVDs analyzed), but often exhibited structural deformations and even inverted

orientations in *sspo*^{dmh4/+} mutants ($N = 8$ fish; $n = 22/29$ IVDs appeared abnormal). Arrows (**h**) highlight sites of *sspo*^{dmh4/+} IVL deformation in the transverse plane. Sequential images (3.6 μ m step) through the coronal plane of wildtype (**c–c''**) and *sspo*^{dmh4/+} (**g–g''**) zebrafish highlight the highly deformable structure of *sspo*^{dmh4/+} mutant IVLs. Scale bars = 20 μ m (**c**, **g**); 50 μ m (**b**, **d**, **f**, **h**); 100 μ m (**a**, **e**). IVL intervertebral ligament, AF annulus fibrosus equivalent, NP nucleus pulposus equivalent.

To determine whether elevated spine stiffness represents a generalizable feature of zebrafish scoliosis, or a property specific to *sspo*^{dmh4/+} mutants, we performed SWE on two additional AIS models (*katnb1* and *vangl2*) that share upstream CSF homeostasis defects but differ in underlying molecular genetic causes^{21,22}. Again, significantly faster shear wave velocities were observed in scoliotic *katnb1* and *vangl2* mutants compared to control siblings (Supplementary Fig. 10). Therefore, our results demonstrate altered viscoelastic properties of the zebrafish scoliotic spine that parallel elevated intervertebral disc stiffness observed in human AIS patients^{33,34}.

Oxidative stress-induced spine stiffness is a prognostic biomarker of scoliosis

Shear wave velocities varied noticeably within *sspo*^{dmh4/+} mutant cohorts (Fig. 5c, d). Since the penetrance (Supplementary Fig. 1k) and severity of spinal curvature is also variable among *sspo*^{dmh4/+} zebrafish¹⁵,

we hypothesized that differences in shear wave velocity/spine stiffness may directly reflect scoliosis severity. Using a second cohort of 21 dpf *sspo*^{dmh4/+} mutants (average SL = 8.2 \pm 0.7 mm), we performed μ CT imaging after SWE and performed Cobb-angle measurements of the largest spinal curvature in each animal, which is a biomarker of scoliosis severity. Remarkably, a significant and positive correlation between shear wave velocity and Cobb-angle/curve severity was observed ($R = 0.835$; Fig. 5e).

Elevated spine stiffness was measured after scoliosis onset and could therefore have developed as a consequence of spinal curvature. To determine the relationship between stiffness and scoliosis, we next conducted SWE on *sspo*^{dmh4/+} and wildtype fish at 10 dpf (average SL = 4.7 \pm 0.4 mm), prior to obvious morphological phenotypes (Fig. 1a, b). Remarkably, *sspo*^{dmh4/+} mutant spines were significantly stiffer than wildtype controls before scoliosis onset, suggesting a causal relationship (Fig. 5f). To determine whether elevated tissue

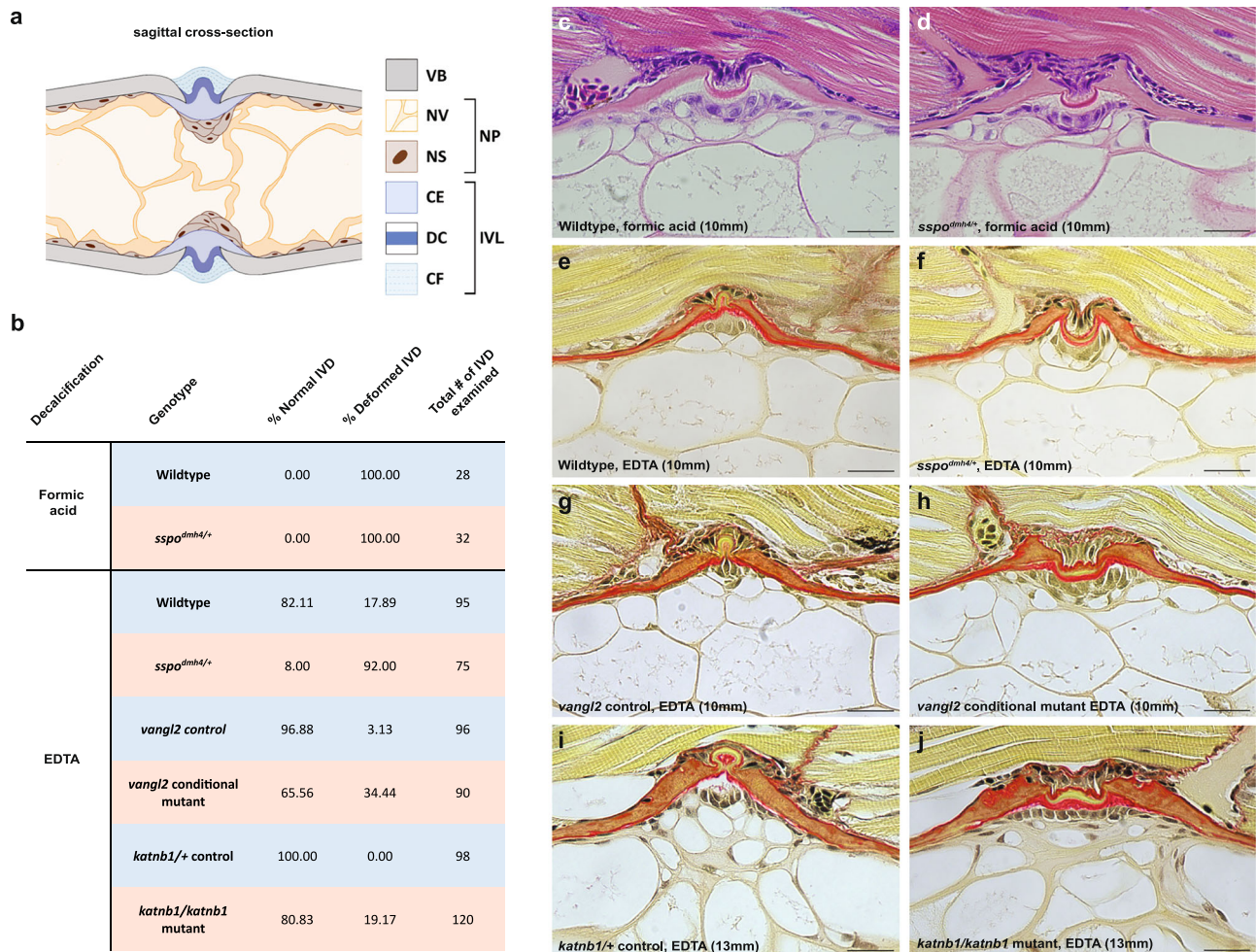


Fig. 3 | Histological analysis of IVL deformations within multiple zebrafish AIS models. a Schematic demonstrating the normal structure and organization of zebrafish IVDs at 21 dpf (10 mm SL) in the sagittal plane. VB vertebra body, NV notochord vacuole, NS notochord sheath cell, CE collagen type II and elastin matrix, DC dense collagen type I matrix, CF collagen type I bundle fiber, NP nucleus pulposus, IVL intervertebral ligament. This schematic is an original image created by Xu, R. (2025) with Tayasui Sketches. **b** Percentage of normal IVDs, deformed

IVDs, and total number of IVDs examined for each genotype, using Formic Acid vs. EDTA decalcification regimens, demonstrating that scoliotic models exhibited higher rates of IVL deformation when compared to their normal sibling controls. **c–j**, Representative H&E and PSR stained images of IVLs for *sspo* (wildtype $N = 8$, $n = 95$, mutant $N = 8$, $n = 75$), *katnb1* (heterozygotes $N = 4$, $n = 98$, homozygotes $N = 6$, $n = 120$), and *vangl2* (control $N = 6$, $n = 96$, conditional mutant $N = 6$, $n = 90$) models, scale bar = 20 μm .

stiffness was linked to elevated oxidative stress, zebrafish were treated with 500 μM of NACET from 5 to 10 dpf, prior to SWE. Strikingly, NACET treatment had no effect on wildtype control animals, but fully suppressed abnormal spine stiffness in *sspo^{dmh4/+}* zebrafish to wildtype levels (Fig. 5f). Similarly, NACET treatment reduced abnormal spine stiffness in *katnb1* zebrafish (Supplementary Fig. 10b). Together, these results directly link oxidative stress to altered viscoelastic properties of the scoliotic spine and identify elevated spine stiffness as a prognostic biomarker of spinal curvature in zebrafish AIS models.

IVD matrix defects precede scoliosis and are directly linked to oxidative stress

IVD deformations and collagen remodelling defects were observed after scoliosis onset in *sspo^{dmh4/+}* mutants and could therefore reflect either the cause or the consequences of spinal curvature. Although SWE indicates structural defects likely precede scoliosis, it lacks sufficient spatial resolution to identify affected tissues. To further investigate whether ultrastructural ECM defects drive spinal curvature in *sspo^{dmh4/+}* models, we performed transmission electron microscopy (TEM) on 10 dpf zebrafish (5 mm SL) prior to an obvious morphological phenotype (Fig. 1a, b). Specifically, we focused on mineralized and cartilaginous domains of the peri-notochordal ECM

that template vertebral centra and IVD development, respectively (Fig. 6a).

In wildtype animals, a uniform layer of collagen ECM was observed within cartilaginous domains, with bundles of collagen fibers organized circumferentially around the notochord projecting out of the sagittal plane of sectioning (Fig. 6c, c'). In contrast, *sspo^{dmh4/+}* cartilaginous segments exhibited irregularities in the thickness and orientation of collagen ECM layers (Fig. 6d, d'). Quantification of collagen ECM thickness (Fig. 6b) revealed that while the minimum thickness in any IVD segment was consistent between wildtype and *sspo^{dmh4/+}* IVD segments, the maximum thickness and local max/min ratios were significantly higher in *sspo^{dmh4/+}* mutants (Fig. 6g–i). Furthermore, the ECM appeared disorganized and misoriented in developing *sspo^{dmh4/+}* IVD segments, with collagen fiber bundles observed running parallel to the sagittal plane (Fig. 6d, d'). Similar ECM thickness defects and collagen fibril disorganization defects were observed in *vangl2* mutant AIS models at 10 dpf (Supplementary Fig. 11a–d, g). Although the penetrance and severity of ECM phenotypes varied among IVD segments from any given animal (Fig. 6g–i), all *sspo^{dmh4/+}* fish ($N = 9$) exhibited IVD defects. Notably, collagen ECM defects were specific to IVDs and were not observed in mineralizing vertebral segments of *sspo^{dmh4/+}* or *vangl2* mutant models (Supplementary Figs. 11e, f, h and 12).

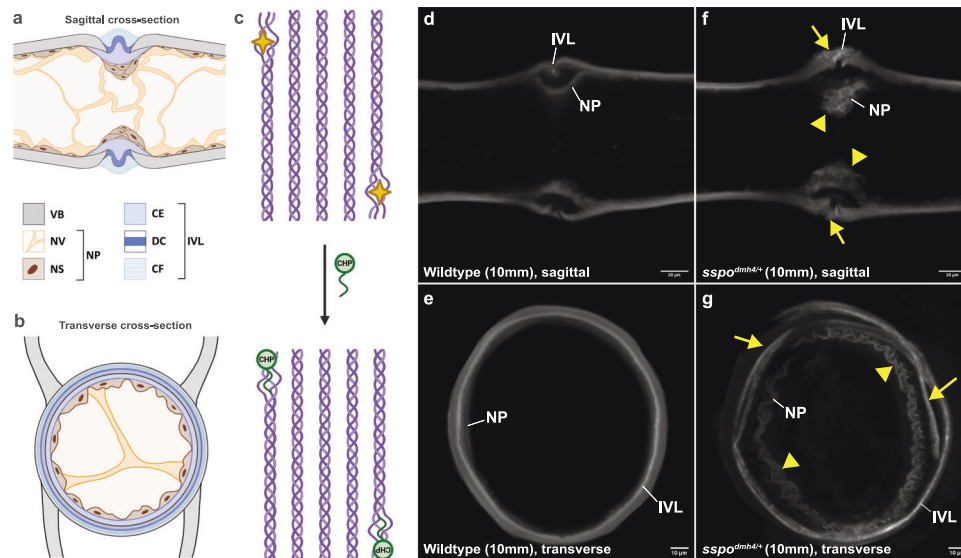


Fig. 4 | *sspo*^{dmh4/+} IVDs exhibit collagenous ECM damage and matrix remodelling. **a, b** Schematic representing the normal structure and organization of zebrafish IVDs at 21 dpf (10 mm SL) in the sagittal (**a**) and transverse (**b**) planes. VB vertebra body, NV notochord vacuole, NS notochord sheath cell, CE collagen type II and elastin matrix, DC dense collagen type I matrix, CF collagen type I bundle fiber, NP nucleus pulposus, IVL intervertebral ligament. This schematic is an original image created by Xu, R. (2025) with Tayasui Sketches. **c** Schematic depicting the mechanism by which collagen-hybridizing peptide (CHP, green probe) integrates into open regions (yellow stars) of collagen fibril triple helices (purple) to report on collagen ECM damage and remodelling. Created in BioRender. Ciruna, B. (2025)

<https://BioRender.com/7k495f0>. **d–g** Confocal images of CHP-stained vertebral and IVD segments at 21 dpf (10 mm SL). **d, e** CHP staining in wildtype animals demonstrates normal remodelling of the collagen ECM matrix within the NP and AF, as seen in sagittal (**d**, $N = 12$, $n = 12$; scale bar = 20 μm) and transverse (**e**, $N = 13$, $n = 13$; scale bar = 10 μm) planes. **f, g** In contrast, *sspo*^{dmh4/+} mutant animals exhibit ectopic CHP staining within NP (arrowheads) and IVL (arrows) structures, as seen in sagittal (**f**, $N = 12$, $n = 12$, scale bar = 20 μm) and transverse (**g**, $N = 15$, $n = 15$, scale bar = 10 μm) planes, indicating significant damage to the collagenous ECM matrix of *sspo*^{dmh4/+} mutant IVDs.

To determine whether collagen ECM defects are also linked to the elevated oxidative state observed around the IVD of *sspo*^{dmh4/+} mutants, zebrafish were treated with 500 μM NACET from 5 to 10 dpf, prior to TEM imaging. Strikingly, NACET treatment had no effect on collagen matrix organization in wildtype animals but restored collagen fiber orientation and suppressed ECM thickness in *sspo*^{dmh4/+} mutants to wildtype levels (Fig. 6e–i). Together, these results demonstrate that oxidative stress-induced collagen ECM defects, specific to IVD segments, precede scoliosis onset in zebrafish AIS models and may therefore be functionally linked to IVL deformations and idiopathic-like spinal curvature.

Discussion

Despite the oxi-inflammatory origins of scoliosis in zebrafish models^{14–16}, we demonstrate that pathogenic mechanisms ultimately converge on a historical focus of human AIS studies—the IVD. Trueta (1968) first reported that morphological deformations of the IVD contribute greatly to AIS spine deformity³⁷, and Harrington (1977) theorized that loss of physical properties (collagen) of the IVD might thus present as a common denominator in AIS³⁸. These ideas have since been explored, in part, by longitudinal radiographic studies of AIS patients associating IVD wedging with the early presentation and progression of spinal curvature^{39,40}, and mathematical modeling of AF collagen fiber imbalance as an etiological factor in scoliosis⁴¹. Although biochemical and histological studies have also identified irregular collagen and elastic properties in IVDs isolated from AIS patients^{42–44}, these defects were observed only after scoliosis onset. Here, we provide direct evidence that ROS-induced IVD stress responses, altered viscoelastic properties, and collagen ECM defects all precede spinal curvature in *sspo*^{dmh4/+} zebrafish. Interestingly, Creb3l2/Bbf2h7, a transmembrane bZIP transcription factor, can be activated by oxidative/ER stress and has been shown in medaka and zebrafish to regulate the expression of COPII component genes for collagen export in the notochord^{43,46}. Although it remains to be determined how oxidative stress ultimately perturbs collagen matrix development (i.e., via

abnormal protein translation, trafficking, cross-linking, etc.) our data, together with published reports, strongly support a causal role for IVD ECM remodelling defects in the etiopathogenesis of scoliosis and highlight the relevance of zebrafish AIS models for pathomechanism discovery and therapeutic development.

At present, genetic screening appears to be ineffective for pre-onset diagnosis of AIS⁴⁷. Diagnosis can only be made after scoliosis onset, and high variability in severe curve progression makes it difficult to predict which patients may ultimately require bracing or surgical intervention. Here, we demonstrate the prognostic capabilities of SWE in zebrafish AIS models. Strikingly, we have determined that elevated spine stiffness can be detected prior to scoliosis onset. As our data complements clinical SWE studies demonstrating elevated AF stiffness in affected AIS patients^{33,34}, spine stiffness in *sspo*^{dmh4/+} zebrafish might similarly be caused by observed IVD collagen remodelling defects. Indeed, spine stiffness and IVD matrix defects are both oxidative stress-dependent and mechanistically linked in *sspo*^{dmh4/+} models, and increases in the thickness and isotropy of a medium (as observed for *sspo*^{dmh4/+} collagen IVD matrix) are predicted to elevate medium stiffness^{48,49}. Although the spatial and molecular origins of elevated stiffness in *sspo*^{dmh4/+} zebrafish remain to be determined, our data provide proof-of-concept that spine stiffness might be explored as a prognostic biomarker for AIS development. Given that SWE is a non-invasive imaging technique that is widely applied in the clinic, clinical translation of these findings could hold tremendous potential to identify patients at high risk of severe scoliosis for earlier, non-surgical intervention.

The oxidative stress-induced origin of ECM defects identified in zebrafish AIS models is equally deserving of clinical consideration. AIS is a common pediatric disorder¹. Nevertheless, it is estimated that <5% total genetic variance in AIS has been determined¹⁰, and genetic associations with cartilaginous ECM and IVD development account for only a subset of these cases^{2–4}. However, environmental variables like infection, diet, lifestyle and microbiome composition can profoundly influence ROS levels^{50–52} and could therefore play a

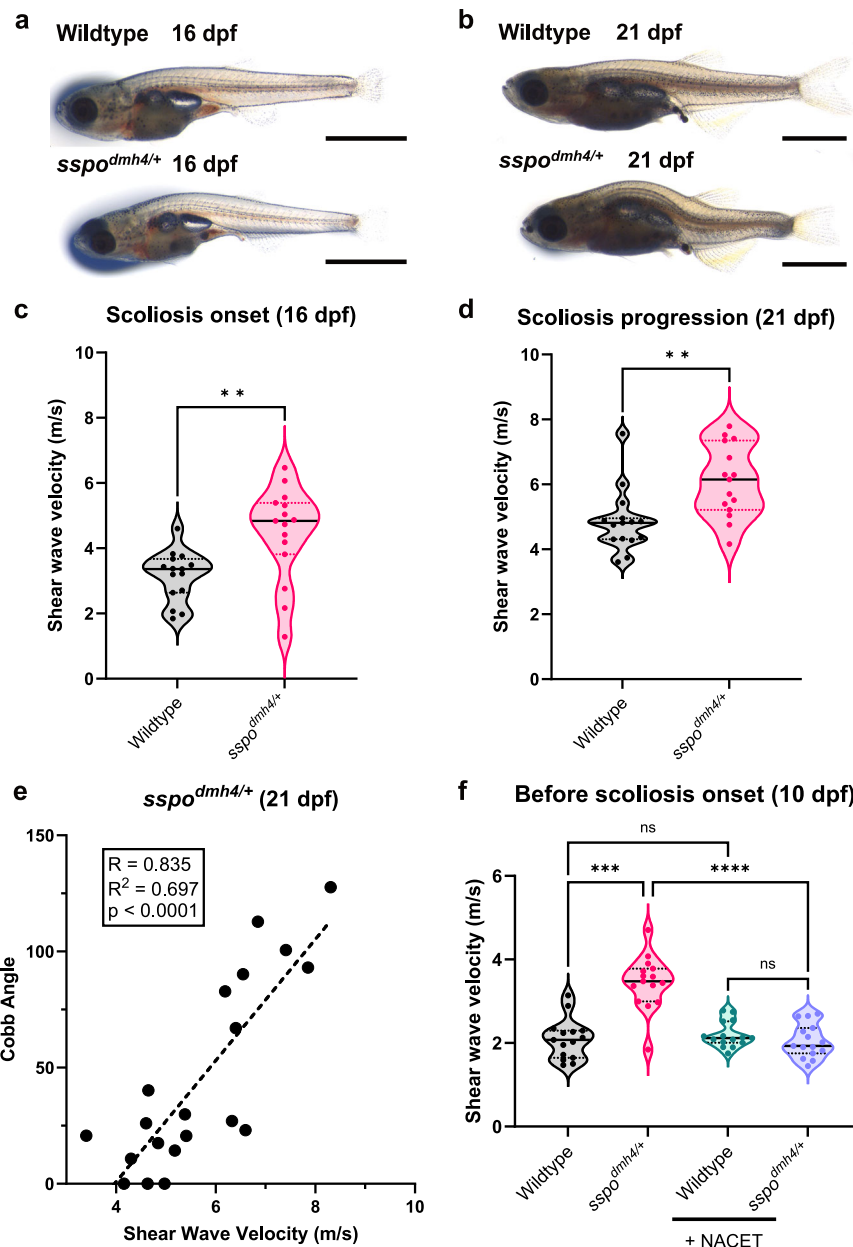
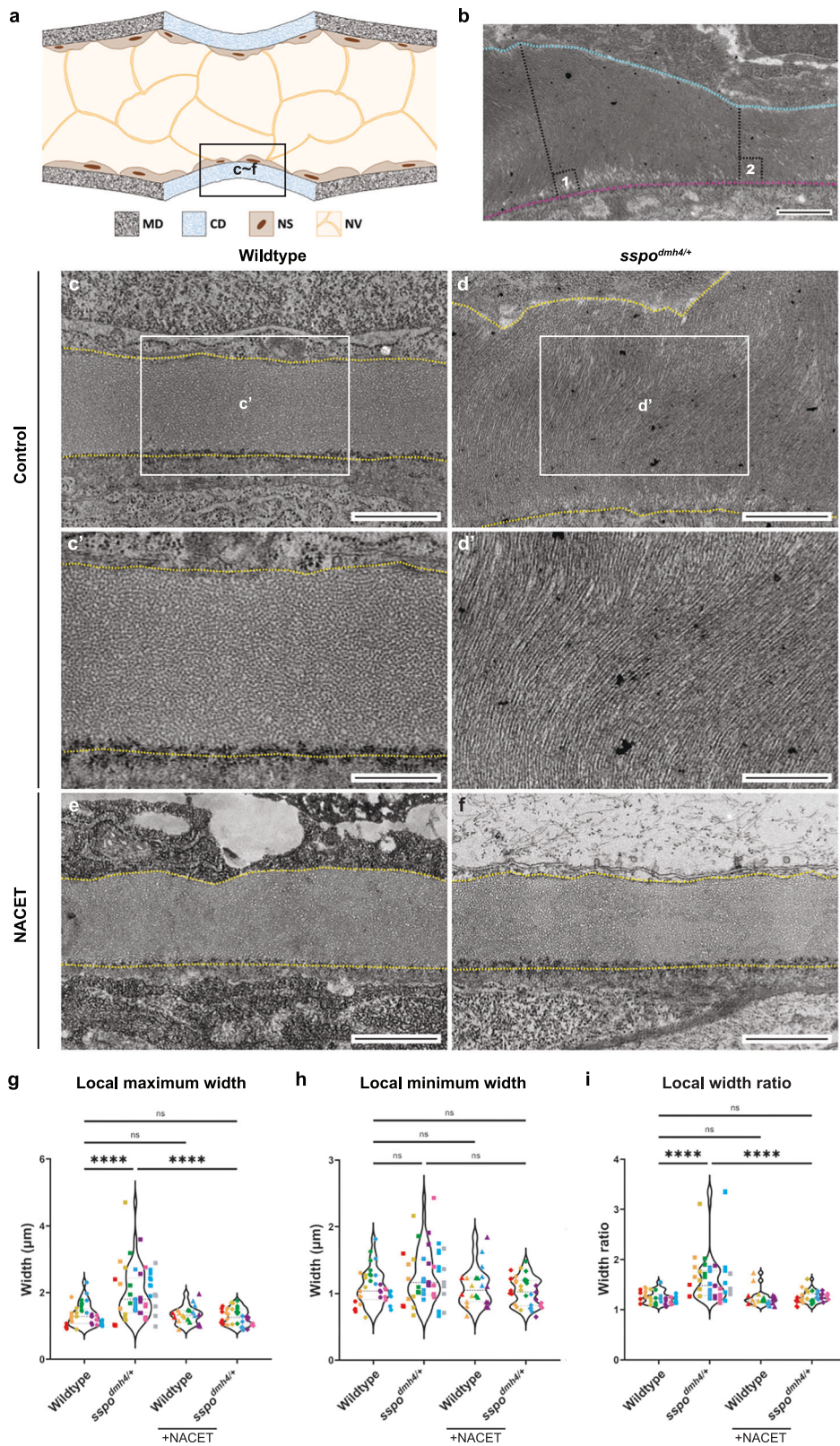


Fig. 5 | Elevated spine stiffness is observed prior to scoliosis onset, positively correlates with curve severity, and is fully suppressed by antioxidant therapy. **a, b** Lateral wholemount images of wildtype and scoliotic *sspo^{dmh4/+}* mutant zebrafish at 16 dpf (**a**, SL = 7.1 ± 0.2 mm) and 21 dpf (**b**, SL = 8.9 ± 0.6 mm). Scale bar = 2 mm. **c, d** Quantification of shear wave velocity measured by SWE along the spine of 16 dpf (**c**) and 21 dpf (**d**) zebrafish, demonstrating significantly greater shear wave velocity and thus spinal stiffness in *sspo^{dmh4/+}* mutant animals. **c** *N* = 15 fish for each genotype. **d** *N* = 15 fish for each genotype. **e** Positive correlation between scoliosis severity (most severe Cobb-angle in sagittal or coronal plane) and spinal stiffness (shear wave velocity) in 21 dpf *sspo^{dmh4/+}* zebrafish, post-curve onset

(*N* = 20). Data was analyzed by a simple linear regression ($R = 0.835$, $R^2 = 0.697$, $p < 0.0001$). **f** Quantification of shear wave velocity measured by SWE along the spine of 10 dpf (SL = 4.7 ± 0.4 mm) demonstrates significant elevation of spine stiffness in *sspo^{dmh4/+}* mutant zebrafish, prior to scoliosis (*N* = 15 for each genotype and treatment). Antioxidant treatment (500 μM NACET) fully suppressed spine stiffness in *sspo^{dmh4/+}* mutant zebrafish to wildtype levels. Violin plots show all data points, median (solid line), and quartiles (dotted line). Data were analyzed by a two-sided Mann–Whitney test (**c, d**) or a Kruskal–Wallis test followed by a Dunn’s multiple comparison test (**f**). (ns: non-significant ($p > 0.05$), ** $p \leq 0.01$, *** $p \leq 0.001$, **** $p \leq 0.0001$). Source data are provided as a Source Data file.

pervasive, yet largely unexplored role in AIS pathogenesis. In addition, neuroinflammation and oxidative stress can also have genetic origins (as in *sspo^{dmh4/+}* mutant zebrafish) and should be explored as etiological factors driving human spinal curvature. This includes not only AIS, but other genetically defined disorders that present with both CNS oxi-inflammation and high incidences of developmental scoliosis, like DiGeorge Syndrome^{53,54}, Rett Syndrome^{55,56}, CDKL5 Deficiency Disorder^{57,58}, and Cerebral Cavernous Malformation^{59,60}.

Finally, regardless of the origins of oxidative stress, prophylactic and therapeutic administration of antioxidants has proven remarkably effective in preventing the onset and severe progression of scoliosis in zebrafish AIS models^{14–16}. Furthermore, we have demonstrated that ER stress responses, elevated spine stiffness and collagen ECM defects in *sspo^{dmh4/+}* mutants, which are all functionally linked to spinal curvature, can be fully suppressed by NACET treatment. If oxidative stress-induced ECM remodelling defects prove relevant to patient populations, then translation of these



findings could have a profound impact on the future management and prevention of human spinal curvature.

Methods

Zebrafish husbandry

Zebrafish husbandry and experimental protocols were approved by the Hospital for Sick Children's Animal Care Committee (Animal Use

Protocol #1000066437), and all protocols were performed in accordance with Canadian Council on Animal Care guidelines. Wildtype zebrafish from TU strains were used. *sspo^{dmh4}* (15), *katnbl^{mh102}* (21), *vangl2^{sfGFP}* (*hsc170Tg*)²², *Tg(βactin::loxP-mCherry-STOP-loxp-zGrad)* (*hsc185Tg*)²², *Tg(foxj1a::iCre)* (*hsc105bTg*)¹⁴, *TgBAC(tnfx::GFP)*¹⁸, *Tg(mpegl::mCherry)*¹⁹, and *TgBAC(col2a1a::eGFP)*²⁶ mutant and transgenic fish used in this study have been previously described.

Fig. 6 | Oxidative stress-induced ECM matrix defects precede scoliosis onset. **a** Schematic of zebrafish notochord development at 10 dpf (5 mm SL) showing cartilaginous ECM domains (IVD), mineralized domains (vertebra), notochord vacuole and notochord sheath cells. This schematic is an original image created by Xu, R. (2025) with Tayasui Sketches. **b** Maximum and minimum ECM widths were measured from lines drawn from the apical surface (cyan dash), perpendicular to the basal surface (magenta dash), at the widest (1) and the narrowest (2) regions within the image, respectively, scale bar = 1 μ m. **c, d** Representative transmission electron micrographs of the collagenous ECM in developing IVDs of 10 dpf (5 mm SL) wildtype (**c**) and *sspo^{dmb4/+}* (**d**) larvae, scale bar = 1 μ m, with respective magnified regions for wildtype (**c'**) and *sspo^{dmb4/+}* (**d'**) scale bar = 500 nm. **e, f** Antioxidant treatment (500 μ M NACET) had no effect on wildtype ECM development (**e**) but suppressed irregular collagen ECM thickness and fiber orientation phenotypes in *sspo^{dmb4/+}* mutant animals (**f**), scale bar = 1 μ m. **g–i** Quantification of matrix thickness

showed no difference in local minimum ECM widths (**g**), but significant differences between wildtype ($N = 8, n = 36$) and *sspo^{dmb4/+}* mutants ($N = 9, n = 47$) in maximum local thickness (**f**) and local thickness ratios (**h**). ECM thickness of *sspo^{dmb4/+}* mutant IVDs ($N = 7, n = 35$) was restored to wildtype levels upon NACET treatment, while NACET treatment had no effect on wildtype IVD properties ($N = 6, n = 22$). Box plots show all data points, median, and min to max whiskers. Points of the same color belong to the same fish, demonstrating variations in phenotype severity among IVD segments of individual *sspo^{dmb4/+}* fish. Violin plots show all data points; each dot represents a measurement from a single cartilaginous domain, and points with the same color came from the same fish. Data were analyzed by the Kruskal–Wallis test followed by a Dunn's multiple comparison test (ns: non-significant $p > 0.05$, $*p \leq 0.05$, $**p \leq 0.01$, $***p \leq 0.001$, $****p \leq 0.0001$). Source data are provided as a Source Data file.

Information on newly developed transgenic fish *Tg(col2a1a::xbp1δ-eGFP)* can be found below in the “Transgenesis” method section. Embryos from natural matings were grown at 28.5 °C. When required, experimental animals were euthanized with tricaine (500 mg/L; MS-222/MESAB), followed by submersion of anesthetized fish in ice water for several minutes. As laboratory zebrafish strains do not utilize a chromosomal sex determination mechanism and sex differentiation does not initiate until after ~3 weeks post-fertilization⁶¹, we cannot report sex for our embryonic and larval studies.

Zebrafish genotyping

Genotyping protocols have been described previously and can be found in the following publications: *sspo^{dmb4/+}*⁽¹⁵⁾, *katnbl^{1mh102/mh102}*⁽²¹⁾, *vangl2^{sfGFP/sfGFP}*⁽²²⁾. Primer sequences used for genotyping can be found in Supplementary Table 1.

Conditional degradation of sfGFP-Vangl2

To conditionally disrupt Vangl2 activity, the zGrad anti-EGFP nanobody protein degradation system was used to degrade sfGFP-Vangl2 protein (*vangl2^{sfGFP/sfGFP}* line) specifically within motile-ciliated lineages of the brain and spinal cord. Briefly, a previously generated and ubiquitously expressed *Tg(β-actin2::loxP-mCherry-STOP-loxP-zGrad)*²² transgene was crossed to the *Tg(foxj1a::iCre)* line¹⁴, expressing Cre recombinase (activating zGrad) specifically within motile-ciliated cell lineages of *vangl2^{sfGFP/sfGFP}* animals. See ref. 22 for more detailed information.

Transgenesis

Entry plasmids were generated through BP recombination into respective pDONR plasmids (Invitrogen) and then cloned into standard Tol2 kit Gateway compatible vectors using LR recombination methods to create the final transgenes⁶². To generate *Tg(col2a1a::xbp1δ-eGFP)*, a previously generated p5E-*col2a1a*⁶³, pME-*xbp1δ-eGFP* (obtained by cloning the *xbp1* partial sequence using Gateway primers, detailed in Table 1, from *eflα::xbp1δ-gfp* plasmid²⁴ graciously provided by Dr. Shao Jun Du), and p3E-polyA⁶² were recombined into pDEST Tol2 HR2 transgenesis vector. Embryos were injected at the one-cell stage with 25 pg of Tol2 transposase RNA and 25 pg of the transgene (plasmid). Injected embryos were then screened at 48 hpf for transgenesis marker expression. Imaging of reporter expression was performed on an Axio Zoom.V16 (Zeiss). Embryos displaying strong reporter expression were grown to adulthood and crossed to wild-type fish to establish stable F1 lines. F1 lines were then bred into *sspo^{dmb4/+}* and maintained in *sspo^{dmb4/+}* fish.

DCFH-DA staining

Zebrafish were collected and placed in 12-well plates containing 2 mL of 5 μ M DCFH-DA (Sigma) in E3 media. Plates were kept in the dark and incubated for 15 min (5 dpf zebrafish) or 30 min (10 to 14 dpf zebrafish) at a temperature of 28.5 °C. Zebrafish were then washed three times with E3 media for 5 min each and immediately imaged.

DCFH-DA, *Tg(col2a1a::xbp1δ-eGFP)*, *TgBAC(entpd5a::pkRed)*, *TgBAC(trfα::eGFP)*, and *Tg(mpeg1::mCherry)* imaging

Experimental zebrafish were anesthetized with tricaine (500 mg/L) before imaging. 5 dpf, 10 dpf, or 14 dpf zebrafish were mounted dorsally or laterally in 0.8% low-melting agarose (BioShop), measured for standard length, and imaged on an LSM 710 confocal microscope (Zeiss).

Collagen-hybridizing peptide

Juvenile zebrafish were collected at 21 dpf (10 mm SL) and euthanized with tricaine (500 mg/L) on ice. Euthanized fish were fixed with 100% methanol at -20 °C for 48 h, then rehydrated with 1xPBS before the skin was gently removed with a pair of dissection forceps. Collagen hybridizing peptide (F-CHP from 3Helix, diluted in 1xPBS to 20 μ M) was heated to 80 °C for activation, followed by quenching on an ice block down to room temperature. Fish were immersed in CHP for 48 h at 4 °C in the dark. After CHP staining, fish were transferred into individual tubes for soft tissue lysing in 2%KOH/ethylene glycol/1xPBS solution, then switched to 1%KOH/ethylene glycol/1xPBS when the vertebrae were exposed. Samples were placed on a nutator during tissue lysing until most of the muscle, spinal cord and ventral vasculature had been digested, then cleared with glycerol before imaging on an LSM 710 confocal microscope (Zeiss).

Transmission electron microscopy

Fish were collected at 10 dpf (5 mm SL) and euthanized with tricaine (500 mg/L) on ice. Euthanized samples were fixed in 2% paraformaldehyde and 2.5% glutaraldehyde in 0.1 M sodium cacodylate buffer for 2 h at room temperature, then transferred to 4 °C overnight. Rinsed in buffer, post-fixed in 1% osmium tetroxide in buffer for 90 min, dehydrated in a graded ethanol series (50%, 70%, 90% and 100%, 20 min each step) followed by two propylene oxide changes for 30 min, and embedded in Quetol-Spurr resin. Blocks were cured overnight in the oven at 60 °C. Fish were cut along the sagittal plane 100 μ m deep into the sample. Sections 70 nm thick were cut on a Leica EM UC7 ultramicrotome, and post-stained with 2% uranyl acetate and 3% lead citrate for 20 min each and washed for 5 min after each staining. Sections were air-dried at room temperature before being imaged with a Hitachi HT7800 transmission electron microscope.

Synchrotron μ CT imaging, reconstruction, and segmentation

Juvenile zebrafish were collected at 21 dpf (10 mm SL) and euthanized with tricaine (500 mg/L) on ice. Euthanized fish were fixed with 4% PFA at 4 °C overnight, then washed with 1xPBS before being stained in I2E solution (1% iodine metal in 100% ethanol) overnight at room temperature. Samples were then washed again with 1xPBS to remove excess I2E stain, then mounted in 1.5% agarose in R.O. water in 0.2 mL tubes. Synchrotron μ CT was performed at the bending magnet beamline of BioMedical Imaging and Therapy beamlines (BMIT-BM) at the Canadian Light Source⁶⁴. The beamline is operated in filtered white

mode; therefore, it is essential to filter the beam sufficiently to prevent radiation damage to the sample and agarose gel. Filters of 1.76 mm Al and 0.275 mm Sn were used. Detector was an indirect X-ray microscope (Optique Peter, France) combined with a sCMOS PCO Edge 5.5 camera (PCO, Germany), a 20x objective, and a 4 μm LSO:Tb scintillator to obtain an effective pixel size of 0.360 μm . Generally, the dimension of scanned samples was 400 x 600 x 750 μm^3 . 1500 projections over 180 degrees were collected at an exposure time of 1.5 s. The sample was 25.7 m from the source, and the propagation distance was 3 cm. Phase retrieval and image reconstructions were done using the tolu reconstruction package⁶⁵.

NACET treatments

Fish were housed off-system in 500 mL of 300 mg/L Instant Ocean Sea Salt-treated water in 1.8 L tanks with 12 fish per tank. Water was changed once per day. N-acetyl-L-cysteine ethyl ester (NACET, BOC Sciences Cat# B0689-029481) was prepared as a 250 mM stock solution in 300 mg/L Instant Ocean Sea Salt dissolved in MiliQ water. NACET was administered with water changes once per day at a final concentration of 500 μM . NACET treatment occurred over the course of 5 days, starting at 5 dpf with *sspo*^{dmh4/+} fish and at 12 dpf with *katnbl*^{mhi02/mhi02} fish. The fish were fed in accordance with their regular feed schedule throughout the treatment.

Shear wave elastography (SWE)

Zebrafish spinal tissue stiffness was assessed using an SWE protocol (as described in Supplementary Fig. 8) programmed into a research ultrafast ultrasound system (Vantage 256, Verasonics Inc., Kirkland, WA, USA) with a linear ultrasound probe (L22-14vX, 18 MHz center frequency). Euthanized zebrafish were mounted ventrally in a 35 mm x 10 mm dish (Corning) filled with 1.5% low-melting agarose (BioShop). The probe was positioned longitudinally, dorsal to the zebrafish, in contact with ultrasound gel applied to agarose-embedded samples. The SWE protocol for a single acquisition consisted of two steps: 1) the induction of an acoustic radiation force through a focused ultrasound beam at a push depth between 4 and 9 mm aimed at the center of the zebrafish spine, resulting in a transient perturbation of the tissue and shear waves propagation; 2) an ultrafast Doppler sequence was created with coherent compound plane wave imaging consisting of 3 plane waves (range -3 degrees to +3 degrees, 3-degree steps) with a pulse repetition frequency of 28 kHz. Coherent compounding of the plane waves was applied using a sliding window method as in Kang et al. (window size 3, corresponding to the 3 different titled plane waves, and window step of 1), enabling a virtual framerate of 28kHz⁶⁶. Each acquisition lasted 10 milliseconds. Three acquisitions were collected per zebrafish. After scans were complete, the ultrafast imaging data were streamed to an internal network and then post-processed offline using MATLAB 2019a (The MathWorks Inc., Natick, MA, USA). Tissue velocity data were computed using a Doppler-based autocorrelation estimator, from which tissue velocity maps were reconstructed and presented as a space-time matrix showing shear wave propagation within a specific region of interest. The mean of these shear wave velocities was computed and used as a surrogate for spine stiffness (derived from the shear modulus)⁶⁷.

μCT scanning, reconstruction, and density analysis

Zebrafish were euthanized at 4mpf and fixed in 10% neutral-buffered formalin (Sigma-Aldrich). Fish were mounted in tubes using 1% agarose. Scanning was performed with a SkyScan 1275 μCT (Bruker, Kontich, Belgium) using 50 kV and 80 μA , sample rotation of 180°, image rotation steps of 0.2°, frame averaging of 10, exposure time of 55 ms, camera binning of 1 x 1, and using a pixel size of 18 μm . Projection images were reconstructed into cross-sections using SkyScan's NRecon v.1.7.4.6 software (Bruker, Kontich, Belgium) in a range of attenuation coefficients 0–0.25, with a beam-hardening correction of

40%. The reconstructed images were stored as 16-bit TIFF images. Maximum Intensity Projections were generated (ImageJ software) for tissue mineral density analysis. The line selection tool in ImageJ was then used to manually measure the mean gray value within each vertebral centrum, which can be used as a relative measure for tissue mineral density.

Cobb-angle analysis

Lines were drawn parallel to the top and bottom of most displaced vertebrae for each curve. The Cobb angle was then measured as the angle of intersection between lines drawn perpendicular to the original 2 lines¹⁴. Analysis was conducted using ImageJ^{68,69}. Cobb-angle measurements for lateral and dorsal curvatures were summed to obtain a combined Cobb-angle measurement for each fish. Results were graphed, and statistical significance was calculated using GraphPad Prism 10.1.1 (GraphPad Software).

Quantification of DCFH-DA staining, *Tg(col2a1a::xbp16-eGFP)* and *TgBAC(entpd5a::pkRed)*

Using ImageJ Fiji, regions of interest (ROI) were selected to measure the area and integrated density of the ROI (See Supplementary Fig. 1a for ROI examples). The mean gray value of the background was also measured. The corrected total fluorescence (CTF) of the ROI was calculated as follows: *Integrated Density - (Area of ROI x Mean Gray Value of Background)*. CTF values were then calculated relative to wildtype controls by dividing the CTF values by the average CTF wildtype value. Statistical analysis was performed using a Mann–Whitney test or a Kruskal–Wallis test in GraphPad Prism version 10.1.1 (GraphPad Software).

Quantification of *TgBAC(tnfa::GFP)* and *Tg(mpeg1::mCherry)*

Using ImageJ Fiji, cells expressing *TgBAC(tnfa::GFP)* and/or *Tg(mpeg1::mCherry)* were counted in the dorsal telencephalon region of 10 dpf and 14 dpf *sspo*^{dmh4/+} mutants and wildtype siblings as maximum projection images encompassing a Z-range of 72 μm (for 10 dpf fish) and 108 μm (for 14 dpf fish). Statistical analysis was performed using a Mann–Whitney test or a Kruskal–Wallis test in GraphPad Prism version 10.1.1 (GraphPad Software).

Notochord ECM measurements

TEM scans at 6000x and 10,000x were selected for measurements. The ECM widths were taken with ImageJ and defined as the distance from the luminal side of the notochord ECM to the basal side of the notochord sheath (between cyan and magenta dash Fig. 6b). Two measurements were taken from a single scanned image: a local maximum width (the thickest area along the ECM) and a local minimum (thinnest area along the ECM). The local ratio was obtained by dividing the maximum width by its paired minimum width.

Histology

Juvenile zebrafish were collected at 21 dpf (10 mm SL) or 30 dpf (13 mm SL), then euthanized on ice with tricaine (500 mg/L). Euthanized fish were fixed with 4% PFA at 4 °C overnight, then washed with 1xPBS, before decalcification with either EDTA (0.35 M EDTA with gentle rocking at 4 °C for 4 days) or formic acid (Thermo Fisher Scientific CAS: CS511-1D, gentle rocking at RT for 2–3 days). Decalcified samples were processed, put in a mold, embedded with 60 °C liquid paraffin, and transferred to a cooling plate for the wax to freeze. Embedded blocks were sectioned with a microtome, generating ribbons of 3–4 μm thin onto a water bath, then collected onto a slide and dried overnight. Samples were then deparaffinized in xylene (3 x 3 min), transferred to absolute ethanol (3 x 10 dip), 95% ethanol (10 dips), and washed with water. Then, sample processing occurred in the order of celestine blue (5 min), stain in Harris' haematoxylin (5 min), acid alcohol (5 dips), and blue in Scott's tapwater (1 min), with

water-wash between each step. Pico-Sirius Red or H&E were then applied for 30 min, blotted dry, and dehydrated in 100% ethanol (4x), xylene (3x), 10 dips each, before being sealed with a coverslip.

Statistics and reproducibility

Statistical analyses were performed in GraphPad Prism version 10.1.1 (GraphPad Software). Two-tailed, non-parametric Mann–Whitney tests were used for comparisons between two groups, while non-parametric Kruskal–Wallis tests followed by Dunn’s multiple comparisons test were used for analyzing multiple groups. A *p*-value less than 0.05 was considered statistically significant. Statistical test and sample sizes can be found in the Figure legends. Individual *p*-value ranges are indicated in the Figure legends, and exact *p*-values can be found in Supplementary Data 1. The total number of zebrafish analyzed is represented by *N*, and individual data points, such as measured IVDs, are represented by *n* numbers. The detailed number of zebrafish (*N*) and data points (*n*) for each experiment can be found in the respective figure legend.

Reporting summary

Further information on research design is available in the Nature Portfolio Reporting Summary linked to this article.

Data availability

Due to their large size, μ CT imaging files are available upon request. Source data are provided with this paper.

References

- Cheng, J. C. et al. Adolescent idiopathic scoliosis. *Nat. Rev. Dis. Prim.* **1**, 1–21 (2015).
- Wise, C. A. et al. The cartilage matrixome in adolescent idiopathic scoliosis. *Bone Res.* **8**, 1–13 (2020).
- Haller, G. et al. A polygenic burden of rare variants across extracellular matrix genes among individuals with adolescent idiopathic scoliosis. *Hum. Mol. Genet.* **25**, 202–209 (2016).
- Karner, C. M., Long, F., Solnica-Krezel, L., Monk, K. R. & Gray, R. S. Gpr126/Adgrg6 deletion in cartilage models idiopathic scoliosis and pectus excavatum in mice. *Hum. Mol. Genet.* **24**, 4365–4373 (2015).
- Takahashi, Y. et al. A genome-wide association study identifies common variants near LXB1 associated with adolescent idiopathic scoliosis. *Nat. Genet.* **43**, 1237–1240 (2011).
- Su, Z. et al. The mutational landscape of PTK7 in congenital scoliosis and adolescent idiopathic scoliosis. *Genes* **12**, 1791 (2021).
- Patten, S. A. et al. Functional variants of POC5 identified in patients with idiopathic scoliosis. *J. Clin. Invest.* **125**, 1124–1128 (2015).
- Wen, W. et al. Rare variant association analyses reveal the significant contribution of carbohydrate metabolic disturbance in severe adolescent idiopathic scoliosis. *J. Med. Genet.* **61**, 666–676 (2024).
- Wang, X. et al. Impaired glycine neurotransmission causes adolescent idiopathic scoliosis. *J. Clin. Invest.* **134**, e168783 (2024).
- Kou, I. et al. Genome-wide association study identifies 14 previously unreported susceptibility loci for adolescent idiopathic scoliosis in Japanese. *Nat. Commun.* **10**, 3685 (2019).
- Bagnat, M. & Gray, R. S. Development of a straight vertebrate body axis. *Development* **147**, dev175794 (2020).
- Boswell, C. W. & Ciruna, B. Understanding idiopathic scoliosis: a new zebrafish school of thought. *Trends Genet.* **33**, 183–196 (2017).
- Grimes, D. T. et al. Zebrafish models of idiopathic scoliosis link cerebrospinal fluid flow defects to spine curvature. *Science* **352**, 1341–1344 (2016).
- Van Gennip, J. L. M., Boswell, C. W. & Ciruna, B. Neuroinflammatory signals drive spinal curve formation in zebrafish models of idiopathic scoliosis. *Sci. Adv.* **4**, eaav1781 (2018).
- Rose, C. D. et al. SCO-spondin defects and neuroinflammation are conserved mechanisms driving spinal deformity across genetic models of idiopathic scoliosis. *Curr. Biol.* **30**, 2363–2373.e6 (2020).
- Djebar, M. et al. Astrogliosis and neuroinflammation underlie scoliosis upon cilia dysfunction. *eLife*. **13**, RP96831 (2024).
- Soh, N. Recent advances in fluorescent probes for the detection of reactive oxygen species. *Anal. Bioanal. Chem.* **386**, 532–543 (2006).
- Marjoram, L. et al. Epigenetic control of intestinal barrier function and inflammation in zebrafish. *Proc. Natl Acad. Sci.* **112**, 2770–2775 (2015).
- Ellett, F., Pase, L., Hayman, J. W., Andrianopoulos, A. & Lieschke, G. J. mpeg1 promoter transgenes direct macrophage-lineage expression in zebrafish. *Blood* **117**, e49–e56 (2011).
- Wopat, S. et al. Spine patterning is guided by segmentation of the notochord sheath. *Cell Rep.* **22**, 2026–2038 (2018).
- Meyer-Miner, A., Van Gennip, J. L. M., Henke, K., Harris, M. P. & Ciruna, B. Resolving primary pathomechanisms driving idiopathic-like spinal curvature using a new katnb1 scoliosis model. *iScience* **25**, 105028 (2022).
- Jussila, M., Boswell, C. W., Griffiths, N. W., Pumputis, P. G. & Ciruna, B. Live imaging and conditional disruption of native PCP activity using endogenously tagged zebrafish sfGFP-Vangl2. *Nat. Commun.* **13**, 5598 (2022).
- Zhang, Z. et al. Redox signaling and unfolded protein response coordinate cell fate decisions under ER stress. *Redox Biol.* **25**, 101047 (2019).
- Li, J. et al. A transgenic zebrafish model for monitoring xbp1 splicing and endoplasmic reticulum stress in vivo. *Mech. Dev.* **137**, 33–44 (2015).
- Dale, R. M. & Topczewski, J. Identification of an evolutionarily conserved regulatory element of the zebrafish col2a1a gene. *Dev. Biol.* **357**, 518–531 (2011).
- Askary, A. et al. Iroquois proteins promote skeletal joint formation by maintaining chondrocytes in an immature state. *Dev. Cell* **35**, 358–365 (2015).
- Kague, E. et al. 3D assessment of intervertebral disc degeneration in zebrafish identifies changes in bone density that prime disc disease. *Bone Res.* **9**, 39 (2021).
- Gistelincq, C. et al. Zebrafish type I collagen mutants faithfully recapitulate human type I collagenopathies. *Proc. Natl Acad. Sci. USA* **115**, E8037–E8046 (2018).
- Symmons, S. Notochordal and elastic components of the axial skeleton of fishes and their functions in locomotion. *J. Zool.* **189**, 157–206 (1979).
- Hong, H., Roy, B. C., Chalamaiyah, M., Bruce, H. L. & Wu, J. Pre-treatment with formic acid enhances the production of small peptides from highly cross-linked collagen of spent hens. *Food Chem.* **258**, 174–180 (2018).
- Savi, F. M., Brierty, G. I., Baldwin, J., Theodoropoulos, C. & Woodruff, M. A. Comparison of different decalcification methods using rat mandibles as a model. *J. Histochem Cytochem.* **65**, 705–722 (2017).
- Zitny, J. L. et al. Molecular level detection and localization of mechanical damage in collagen enabled by collagen hybridizing peptides. *Nat. Commun.* **8**, 14913 (2017).
- Langlais, T. et al. Shear-wave elastography can evaluate annulus fibrosus alteration in adolescent scoliosis. *Eur. Radio.* **28**, 2830–2837 (2018).
- Vergari, C. et al. Shear wave elastography of lumbar annulus fibrosus in adolescent idiopathic scoliosis before and after surgical intervention. *Eur. Radiol.* **30**, 1980–1985 (2020).
- Villemain, O. et al. Ultrafast ultrasound imaging in pediatric and adult cardiology: techniques, applications, and perspectives. *JACC Cardiovasc. Imaging* **13**, 1771–1791 (2020).

36. Villalobos Lizardi, J. C. et al. A guide for assessment of myocardial stiffness in health and disease. *Nat. Cardiovasc. Res.* **1**, 8–22 (2022).
37. Trueta, J. in *Studies of the Development and Decay of the Human Frame*. 306–315 (William Heinemann Medical Books Ltd., 1968).
38. Harrington, P. R. The etiology of idiopathic scoliosis. *Clin. Orthop. Relat. Res.* **126**, 17–25 (1977).
39. de Reuver, S. et al. Anterior lengthening in scoliosis occurs only in the disc and is similar in different types of scoliosis. *Spine J.* **20**, 1653–1658 (2020).
40. Will, R. E., Stokes, I. A., Qiu, X., Walker, M. R. & Sanders, J. O. Cobb angle progression in adolescent scoliosis begins at the intervertebral disc. *Spine* **34**, 2782–2786 (2009).
41. Heidari, B., FitzPatrick, D., Synnott, K. & McCormack, D. Modelling of annulus fibrosus imbalance as an aetiological factor in adolescent idiopathic scoliosis. *Clin. Biomech.* **19**, 217–224 (2004).
42. Duance, V. C. et al. Changes in collagen cross-linking in degenerative disc disease and scoliosis. *Spine* **23**, 2545–2551 (1998).
43. Taylor, T. K., Ghosh, P. & Bushell, G. R. The contribution of the intervertebral disk to the scoliotic deformity. *Clin. Orthop. Relat. Res.* **79**, 90 (1981).
44. Yu, J., Fairbank, J. C. T., Roberts, S. & Urban, J. P. G. The elastic fiber network of the annulus fibrosus of the normal and scoliotic human intervertebral disc. *Spine* **30**, 1815–1820 (2005).
45. Ishikawa, T. et al. UPR transducer BBF2H7 allows export of type II collagen in a cargo- and developmental stage-specific manner. *J. Cell Biol.* **216**, 1761–1774 (2017).
46. Melville, D. B. et al. The feelgood mutation in zebrafish dysregulates COPII-dependent secretion of select extracellular matrix proteins in skeletal morphogenesis. *Dis. Models Mech.* **4**, 763–776 (2011).
47. Cheng, T., Einarsdottir, E., Kere, J. & Gerdhem, P. Idiopathic scoliosis: a systematic review and meta-analysis of heritability. *EFORT Open Rev.* **7**, 414–421 (2022).
48. Savage, M. K. Seismic anisotropy and mantle deformation: What have we learned from shear wave splitting?. *Rev. Geophys.* **37**, 65–106 (1999).
49. Villemain, O. et al. Myocardial stiffness evaluation using non-invasive shear wave imaging in healthy and hypertrophic cardiomyopathic adults. *JACC Cardiovasc. Imaging* **12**, 1135–1145 (2019).
50. Bostick, J. W., Schonhoff, A. M. & Mazmanian, S. K. Gut microbiome-mediated regulation of neuroinflammation. *Curr. Opin. Immunol.* **76**, 102177 (2022).
51. Foo, J., Bellot, G., Pervaiz, S. & Alonso, S. Mitochondria-mediated oxidative stress during viral infection. *Trends Microbiol.* **30**, 679–692 (2022).
52. Peters, A., Nawrot, T. S. & Baccarelli, A. A. Hallmarks of environmental insults. *Cell* **184**, 1455–1468 (2021).
53. Homans, J. F. et al. Scoliosis in association with the 22q11.2 deletion syndrome: an observational study. *Arch. Dis. Child* **104**, 19–24 (2019).
54. Menghi, M. et al. Neuroinflammation and oxidative stress in individuals affected by DiGeorge syndrome. *Int. J. Mol. Sci.* **24**, 4242 (2023).
55. Huang, T. J., Lubicky, J. P. & Hammerberg, K. W. Scoliosis in Rett syndrome. *Orthop. Rev.* **23**, 931–937 (1994).
56. Pecorelli, A., Cervellati, C., Hayek, J. & Valacchi, G. OxInflammation in Rett syndrome. *Int. J. Biochem Cell Biol.* **81**, 246–253 (2016).
57. Jagtap, S. et al. Aberrant mitochondrial function in patient-derived neural cells from CDKL5 deficiency disorder and Rett syndrome. *Hum. Mol. Genet.* **28**, 3625–3636 (2019).
58. Mangatt, M. et al. Prevalence and onset of comorbidities in the CDKL5 disorder differ from Rett syndrome. *Orphanet J. Rare Dis.* **11**, 39 (2016).
59. Retta, S. F. & Glading, A. J. Oxidative stress and inflammation in cerebral cavernous malformation disease pathogenesis: Two sides of the same coin. *Int. J. Biochem. Cell Biol.* **81**, 254–270 (2016).
60. Shenkar, R. et al. Exceptional aggressiveness of cerebral cavernous malformation disease associated with PDCD10 mutations. *Genet. Med.* **17**, 188–196 (2015).
61. Kossack, M. E. & Draper, B. W. Genetic regulation of sex determination and maintenance in zebrafish (*Danio rerio*). *Curr. Top. Dev. Biol.* **134**, 119–149 (2019).
62. Kwan, K. M. et al. The Tol2kit: A multisite gateway-based construction kit for Tol2 transposon transgenesis constructs. *Dev. Dyn.* **236**, 3088–3099 (2007).
63. Rebello, D. et al. COL11A2 as a candidate gene for vertebral malformations and congenital scoliosis. *Hum. Mol. Genet.* **32**, 2913–2928 (2023).
64. Gasilov, S. et al. Hard X-ray imaging and tomography at the Biomedical Imaging and Therapy beamlines of Canadian Light Source. *J. Synchrotron. Rad.* **31**, 1346–1357(2024).
65. Faragó, T. et al. Tofu: a fast, versatile and user-friendly image processing toolkit for computed tomography. *J. Synchrotron Rad.* **29**, 916–927 (2022).
66. Kang, J., Jang, W. S. & Yoo, Y. High PRF ultrafast sliding compound Doppler imaging: fully qualitative and quantitative analysis of blood flow. *Phys. Med. Biol.* **63**, 045004 (2018).
67. Taljanovic, M. S. et al. Shear-wave elastography: basic physics and musculoskeletal applications. *Radiographics* **37**, 855–870 (2017).
68. Schneider, C. A., Rasband, W. S. & Eliceiri, K. W. NIH Image to ImageJ: 25 years of image analysis. *Nat. Methods* **9**, 671–675 (2012).
69. Schindelin, J., Rueden, C. T., Hiner, M. C. & Eliceiri, K. W. The ImageJ ecosystem: an open platform for biomedical image analysis. *Mol. Reprod. Dev.* **82**, 518–529 (2015).

Acknowledgements

We gratefully acknowledge the SickKids' Nanoscale Biomedical Imaging Facility for assistance with TEM sample preparation and imaging, the Toronto Center for Phenogenomics for assistance with histological sample preparation, the SickKids' Zebrafish Facility technicians for excellent zebrafish care, Nigel Griffiths for technical assistance, and Dr. Ronald Kwon for support with μ CT TMD analyses. Part of the research described in this paper was performed at the Canadian Light Source, a national research facility of the University of Saskatchewan, which is supported by the Canada Foundation for Innovation (CFI), the Natural Sciences and Engineering Research Council (NSERC), the National Research Council (NRC), the Canadian Institutes of Health Research (CIHR), the Government of Saskatchewan, and the University of Saskatchewan. The following grants supported this work: Canadian Institutes of Health Research Foundation grant FDN-167285 (B.C.). Canada Research Chair Program (B.C.). Canadian Institute of Health and Research Canada Graduate Scholarship FBD-181495 (P.G.P.). Natural Sciences and Engineering Research Council of Canada (NSERC) grant RGPIN-2021-03539 (O.V.). Canadian Institutes of Health Research operating grant 148683 (B.F.E.). The Hospital for Sick Children Research Institute funding (B.C., O.V., D.E.L.).

Author contributions

B.C. and O.V. conceptualized, administered, and supervised the project. P.G.P., R.X., J.G., A.P., V.E., and J.L.M.V.G. performed experiments, data analysis, and visualized the data. P.G.P., R.X., J.G., A.P., V.E., J.L.M.V.G., B.F.E., N.F., J.B., O.V., and B.C. contributed to the methodology of the project. N.F., J.B. created the software for zebrafish SWE analysis. B.C., O.V., P.G.P., B.F.E., D.E.L. acquired funding. P.G.P., R.X., J.G., O.V., and B.C. wrote the original draft of the paper. P.G.P., R.X., J.G., A.P., V.E., J.L.M.V.G., B.F.E., N.F., J.B., D.E.L., O.V., and B.C. reviewed and edited the paper.

Competing interests

The authors declare no competing interests.

Additional information

Supplementary information The online version contains supplementary material available at <https://doi.org/10.1038/s41467-025-63742-2>.

Correspondence and requests for materials should be addressed to Olivier Villemain or Brian Ciruna.

Peer review information *Nature Communications* thanks Juan Melchor, and the other, anonymous, reviewer(s) for their contribution to the peer review of this work. A peer review file is available.

Reprints and permissions information is available at <http://www.nature.com/reprints>

Publisher's note Springer Nature remains neutral with regard to jurisdictional claims in published maps and institutional affiliations.

Open Access This article is licensed under a Creative Commons Attribution-NonCommercial-NoDerivatives 4.0 International License, which permits any non-commercial use, sharing, distribution and reproduction in any medium or format, as long as you give appropriate credit to the original author(s) and the source, provide a link to the Creative Commons licence, and indicate if you modified the licensed material. You do not have permission under this licence to share adapted material derived from this article or parts of it. The images or other third party material in this article are included in the article's Creative Commons licence, unless indicated otherwise in a credit line to the material. If material is not included in the article's Creative Commons licence and your intended use is not permitted by statutory regulation or exceeds the permitted use, you will need to obtain permission directly from the copyright holder. To view a copy of this licence, visit <http://creativecommons.org/licenses/by-nc-nd/4.0/>.

© The Author(s) 2025